Quasi-Deterministic Channel Propagation Model for Human Sensing: Gesture Recognition Use Case

JACK CHUANG [1], **RAIED CAROMI** [1], **JELENA SENIC** [1], **SAMUEL BERWEGER** [2],
NEERAJ VARSHNEY [1,3] **(Senior Member, IEEE), JIAN WANG** [1], **CHIEHPING LAI** [1], **ANURAAG BODI** [1,3],
WILLIAM SLOANE [1,4], **CAMILLO GENTILE** [1] **(Member, IEEE), AND NADA GOLMIE** [2] **(Fellow, IEEE)**

[1] Radio Access and Propagation Metrology Group, National Institute of Standards and Technology, Gaithersburg, MD 20899, USA

[2] Communications Technology Laboratory, National Institute of Standards and Technology, Gaithersburg, MD 20899, USA

[3] Prometheus Computing LLC, Cullowhee, NC 28723, USA

[4] Electrical and Electronic Engineering Department, University of Canterbury, Christchurch 8041, New Zealand

CORRESPONDING AUTHOR: C. GENTILE (e-mail: camillo.gentile@nist.gov)

ABSTRACT We describe a quasi-deterministic channel propagation model for human gesture recognition reduced from real-time measurements with our context-aware channel sounder, considering four human subjects and 20 distinct body motions, for a total of 120000 channel acquisitions. The sounder features a radio-frequency (RF) system with 28 GHz phased-array antennas to extract discrete multipaths backscattered from the body in path gain, delay, azimuth angle-of-arrival, and elevation angle-of-arrival domains, and features camera / Lidar systems to extract discrete keypoints that correspond to salient parts of the body in the same domains as the multipaths. Thanks to the precision of the RF system, with average error of only 0.1 ns in delay and 0.2° in angle, we can reliably associate the multipaths to the keypoints. This enables modeling the backscatter properties of individual body parts, such as Radar cross-section and correlation time. Once the model is reduced from the measurements, the channel is realized through raytracing a stickman of keypoints – the deterministic component of the model to represent generalizable motion – superimposed with a Sum-of-Sinusoids process – the stochastic component of the model to render enhanced accuracy. Finally, the channel realizations are compared to the measurements, substantiating the model's high fidelity.

INDEX TERMS 6G, JCAS, camera, Lidar, joint communications and sensing, 28 GHz, phased-array antennas.

I. INTRODUCTION

THE EVOLUTION of wireless networks from generation to generation over the last 40 years has witnessed ever wider bandwidths, ever more antennas, and ever shorter packet durations, all for the sole purpose of delivering higher communications throughput. As a byproduct, today's networks have fine enough resolution in the respective delay (range), angle (space), and Doppler frequency shift (velocity) domains to enable sensing the contours of relatively small targets such as humans, vehicles, and robots by way of Radar [1]. What is more, the pervasiveness of today's networks – composed from small cells, relays, Wi-Fi routers,

etc., in addition to just cell towers — enables ubiquitous monitoring and tracking of targets for Internet of Things (IoT) applications such as smart home, smart manufacturing, smart transportation, and smart healthcare [2], [3], [4], [5]. The extension of network functionality from communications alone to sensing has paved the way for *joint communications and sensing* (JCAS) as the defining trait of 6G networks. And, as their 5G predecessors expanded operation into the millimeter-wave (mmWave) bands, 6G networks will expand operation into the sub-Terahertz (sub-THz) bands, where bandwidths are projected in the tens of Gigahertz, number of antennas in the thousands, and packet durations in the

hundreds of microseconds, making, for example, resolution of fingers for sign language recognition a reality.

What has remained steadfast over this evolution is the need for accurate channel propagation models for the reliable design and planning of the next-generation network through simulation with hundreds or thousands of nodes. As the complexity of the networks has grown over the last 40 years, this remains truer than ever. The most recent network design — for 5G — was predicated on the 3rd Generation Partnership Project (3GPP) 38.901 channel propagation model [6], a fully stochastic cluster-based model designed to represent propagation in different *environments*, in which each cluster corresponds to a distinct scatter center in the environment – *e.g.*, a building facade outdoors, a wall indoors – that disperses radiated power into discrete multipath components, or simply *multipaths*, each representing a planar wave, that are distributed randomly in the delay, angle, and Doppler domains based on coarse fitting to scant measurements. The model generates tap delay line (TDL) or cluster delay line (CDL) realizations that in turn exhibit random behavior. While sufficient to evaluate communications performance such as throughput, packet delay, and bit error rate, how a target scatters power in these domains in a temporally consistent manner is the very radio-frequency (RF) signature that characterizes a target, so fully stochastic models are inadequate for sensing. Furthermore, the much greater propagation loss in the mmWave and sub-THz bands [7], where the fine resolution that makes sensing possible is available, limits the use cases envisioned for sensing to meters or tens of meters rather than to hundreds or thousands of meters that are typical for communications [8]. At such short ranges the spatial resolution is much finer, and at such high frequencies the target is electrically large — *i.e.*, much larger than the order of a wavelength — so multiple scatter centers from the same target will be resolvable. Thus a target cannot be modeled as a single scatter center.

To address the shortcomings of fully stochastic models, developed to evaluate the performance of communications systems in different environments, not for sensing targets, a number of fully deterministic channel models — which are based on electromagnetic theory, not measurement — that model backscatter from the human body have appeared over the last 15 years. As they predict on a given shape for the body, they are inherently generalizable across a range of body dimensions; and as the shape can evolve over time in dynamic scenarios, they are inherently temporally consistent, which is critical for sensing. In [9], [10], three such models – the triple knife-edge diffraction (TKED), the uniform theory of diffraction (UTD), and physical optics (PO) – are compared in Table 1 (taken from [9]) in terms of runtime, accuracy, and applicability. In particular, the PO model – the most complex of the three – when applied to the so-called "phantom" shape representing the full contour of the body as an infinite number of scatter centers does result in high-fidelity realizations, but is too computationally expensive to simulate large networks with numerous targets.

More recently, *keypoint* models [11], [12], [13], [14], [15], [16] – namely models that represent the human body through a collection of 16 to 21 discrete point scatterers that correspond to salient parts (*e.g.*, head, hands, knees) – have emerged. The keypoints are generated from videos, infrared, and / or Radar of the human in motion. The backscatter from each keypoint is modeled as a specular reflection predicted through simplified raytracing; its path loss is the backscatter loss – referred to as the *Radar cross-section* in the Radar community – added to the free-space propagation loss; how the Radar cross-section is modeled is also described. In [14], [15], [16], in addition, the predictions are compared to measurements at 2.4 GHz and 3.5 GHz for *validation*. And while deterministic models are firmly based on electromagnetic principles, reliability can be attained only through *calibration* — not validation — against measurements.

In the work described here, we adopt the keypoint model for the human body with focus on the gesture recognition use case for enhanced reality applications identified by the *IEEE 802.11bf* task group [17] and the 3GPP systems architecture group [18], among others. What distinguishes our work from the aforementioned citations is, rather than just describe the model or validate it against measurements at *microwave* frequencies, we actually calibrate the model against *mmWave* measurements collected with our state-of-the-art 28 GHz context-aware channel sounder, composed of an RF system for resolving distinct multipaths backscattered from the body and of a camera/Lidar systems for resolving distinct keypoints of the body, all from the same temporally and spatially synchronized measurement. And instead of calibrating a fully deterministic model, our model has a stochastic component – thus we refer to it as a *quasi-deterministic (QD) model* [19], [20], [21] – that captures any deviation of the multipath from the simple specular behavior predicted by the keypoints, enhancing accuracy without compromising the computational efficiency of raytracing. Together with another work of ours [22], we are the first, to our knowledge, to propose a QD channel model for the human body (instead of for environments). How the proposed keypoint model compares to the other models in Table 1 is appended as the last row in the table. The main contributions that we describe in this paper are:

1) A context-aware channel sounder featuring a 28 GHz RF system with a 256-element planar phased-array antenna, 2 GHz bandwidth, and channel acquisition time of only 2.6 ms. It was able to resolve up to 21 distinct multipaths from the body in path gain, delay, azimuth angle-of-arrival (AoA), and elevation AoA per acquisition, with average path gain, delay, and angle errors of only 0.2 dB, 0.1 ns, and 0.2° respectively. The channel sounder also features a camera and a Lidar that can resolve up to 17 keypoints of the body in the same four domains as the multipaths, with all three systems temporally and spatially synchronized to enable comparison of

TABLE 1. Comparison of the proposed keypoint channel model for the human body versus other popular models.

Model	Runtime per simulation	Advantages	Limitations
TKED	Least (≈0.1 sec)	● Fast ● Accurately predicts path gain when the vertical strip is normal to the incident rays	● Cannot model 3D human shapes ● Difficult to scale to 3D propagation scenarios ● Less accurate path gain and delay prediction when compared to the other two methods
UTD	Medium (Modified hexagon with 1 diffraction/ray: ≈2 sec))	● Moderately fast ● Capable of analyzing 3D human shapes ● Scalable to 3D propagation scenarios ● Predicts delay with best accuracy	● Less accurate in path gain prediction when compared to the other two methods
PO	Highest (Human Phantom: ≈8 sec)	● Capable of analyzing full 3D human phantom ● Provides best prediction of human path gain	● Not as scalable as UTD for 3D propagation scenarios due to high computational needs
Keypoint	Least (≈0.1 sec)	● Fast ● Accurately predicts path gain and delay when calibrated against measurement data ● Capable of analyzing 3D human shapes	● May not generalize outside range of measurement scenarios

the resolved multipaths to the resolved keypoints per measurement;

2) An exhaustive measurement campaign including four human subjects with diverse body dimensions, 20 distinct body motions for gesture recognition, and 1500 channel acquisitions for each of the 80 combinations, for a grand total of 120000 channel acquisitions;

3) A QD channel propagation model reduced from the measurements: the deterministic component is provided by a stickman of keypoints that can be scaled to any body dimension to represent generalized motion (beyond the 20 motions in the campaign); the stochastic component is provided by a sum-of-sinusoids (SoS) process to represent the deviation of the multipaths from the keypoints.

The remainder of the paper is developed as follows: In Section II, our context-aware channel sounder and extensive measurement campaign are described, followed in Section III by the methodology we propose to reduce the channel measurements into the QD model. Section IV describes the procedure to generate a channel realization from the model, as well as validation of the model reduced against the measurements. Section V is reserved for conclusions.

II. CHANNEL MEASUREMENT

Section II-A describes our measurement campaign and Section II-B our context-aware channel sounder and how the multipaths and keypoints are extracted from the measurements.

A. MEASUREMENT CAMPAIGN

The measurement campaign mimicked a scenario in which a human is seated on a sofa facing a monitor equipped with a monostatic Radar sensor and moving their hands for gesture recognition by an enhanced reality application. In practice, the measurements were recorded with the human seated on a table facing a transmitter (TX) and a receiver (RX) in a monostatic configuration, as shown in Fig. 1(a).

The heights of the TX and RX antennas were set to 154 cm; the TX and RX antenna printed circuit boards were placed as close as possible to each other (43.4 cm apart) while maintaining their faces in the same plane. A table with adjustable height was used to roughly align the human's shoulders with the boards (although once set, the table height was fixed across all four human subjects despite their different shoulder heights). The TX and RX were placed in a semi-anechoic chamber constructed from absorber, as shown in the figure, but the table itself was outside the chamber.

To account for expected variation in model parameters across different populations, we purposely considered four human subjects with wide ranging body dimensions – two females 160 cm and 168 cm tall and two males 169 cm and 179 cm tall – and 20 different motions for each subject, for a total of 80 cases. Four of the motions were so the sensor could recognize when to start/stop the application: *sitting still*, *standing still*, *standing up*, and *sitting down*. The other 16 motions were specific to gesture recognition while the application is running, with the human sitting and the two hands facing outwards at the shoulder level as the rest position, as shown in Fig. 1(a). From the rest position, the two hands were moved simultaneously, but independently, in four directions to span the full range of motion that is expected for gesturing: *up*, *down*, *left*, and *right*. The measurement period for each case was 3.9 s.

B. CONTEXT-AWARE CHANNEL SOUNDER

The context-aware channel sounder features an RF system to extract multipaths from the measurements, described in 1) below, and camera / Lidar systems to extract keypoints from the measurements, described in 2) below.

1) RF SYSTEM

The TX and RX ends of the system feature 28.5 GHz 8 × 8 phased-array boards of microstrip antennas spaced half-wavelength apart [23] (see Fig. 1(b)). The TX features a
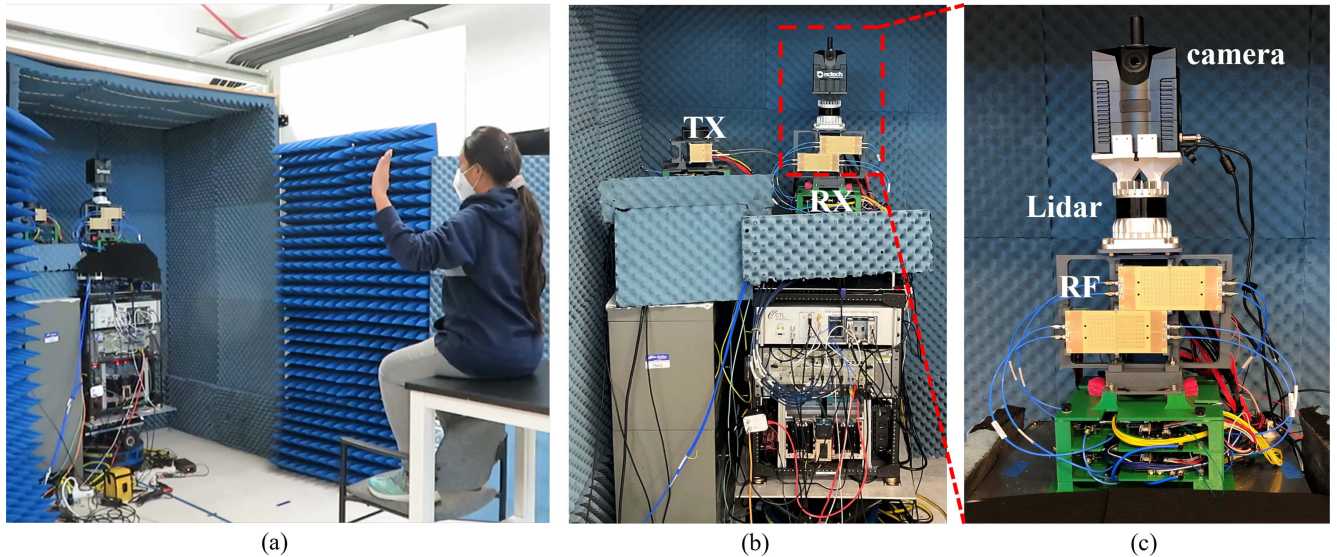
FIGURE 1. Context-aware channel sounder (a) Subject A during the measurement campaign for gesture recognition (b) Monostatic configuration (c) Zoom on RX showing the four stacked 28 GHz 8 × 8 phased-array antennas and the camera and the Lidar mounted above them.

single board only while the RX features four boards stacked in a skew tetromino configuration to increase angular resolution in both dimensions, forming a 256-element antenna array. The configuration was chosen to favor resolution in the azimuth (horizontal) domain over the elevation (vertical) domain while constrained by the connectors on one side of the boards. Extensive simulations were conducted to find the optimal configuration in terms of minimum beamwidth and maximum sidelobe suppression.

To estimate the AoA of multipaths at the RX, we implement *switched beamforming* – a technique we developed to overcome the hardware limitations of the boards [24] – instead of analog beamforming. That is, the channel impulse response (CIR) of each antenna is sampled by switching it on and off sequentially and then the CIRs are beamformed in postprocessing. The two major benefits of switched beamforming are near-ideal beam patterns and short channel sweep duration. When applying a Kaiser taper window across the RX antennas in beamforming, the azimuth and elevation beamwidths are 3.7° and 5.6° respectively. Since the channel that we are characterizing consists of single bounces (from the various body parts), the angle-of-departure from the TX of any multipath can be computed uniquely from its AoA (and delay) [25]. As such, angle-of-departure (AoD) is not estimated to reduce the channel acquisition time. Rather, the 64 antennas at the TX are analog beamformed into a quasi-omnidirectional pattern with 90° azimuth and 50° elevation field-of-view (FoV), equivalent to the FoV of the individual microstrip antennas.

At the TX, the probing signal is a repeated M-ary pseudorandom (PN) sequence with 2047 chips; the chip duration is 0.5 ns, corresponding to a baseband signal bandwidth of 2 GHz. The PN sequence is generated at baseband and modulated at an intermediate frequency (IF) of 4 GHz by an arbitrary waveform generator. The IF signal is fed to the TX antenna board and subsequently upconverted to precisely 28.5 GHz through an on-board mixer, and radiated. An optical cable was used for phase synchronization between the TX and RX and for coordinated switching of the RX antennas at each repeated PN sequence at the TX. At the RX, the received signal at each antenna is downconverted back to IF and directly digitized at 16 Giga samples/s. The digitized signal is then matched filtered with the known PN sequence to generate a complex channel impulse response (CIR) in delay. Predistortion filtering [26] is employed to reduce the delay sidelobes of the matched filtered response to the PN sequence to 47 dB. A channel *acquisition* consists of 256 CIRs (across the RX antennas) acquired every 2.6 ms (385 Hz) during the 3.9 s measurement time for each case, tantamount to 1500 channel acquisitions per case.

In postprocessing, the 256 CIRs of a single acquisition are beamformed every 1° within the FoV of the boards (4500 beams) and then synthesized through the SAGE superresolution algorithm [27] to extract multipaths per time t, indexed as path gain (complex amplitude squared) $PG(t)$, delay $\tau(t)$, azimuth AoA $\theta^A(t)$, and elevation AoA $\theta^E(t)$. SAGE also de-embeds the gain patterns of the microstrip antennas and of the formed beams, ensuring that the estimated properties of the multipaths reflect the channel alone and not the effects of the hardware. Superresolution algorithms nominally yield resolution about five times the inherent beamwidth and/or bandwidth of the system. In fact, the estimated error of the multipath in the four domains was computed against the line-of-sight multipath (as ground-truth) in a controlled experiment with the TX and RX facing each other and with the TX mounted on a mechanical rotator while the RX was static. The probability density function of the measurement error in the four domains across the
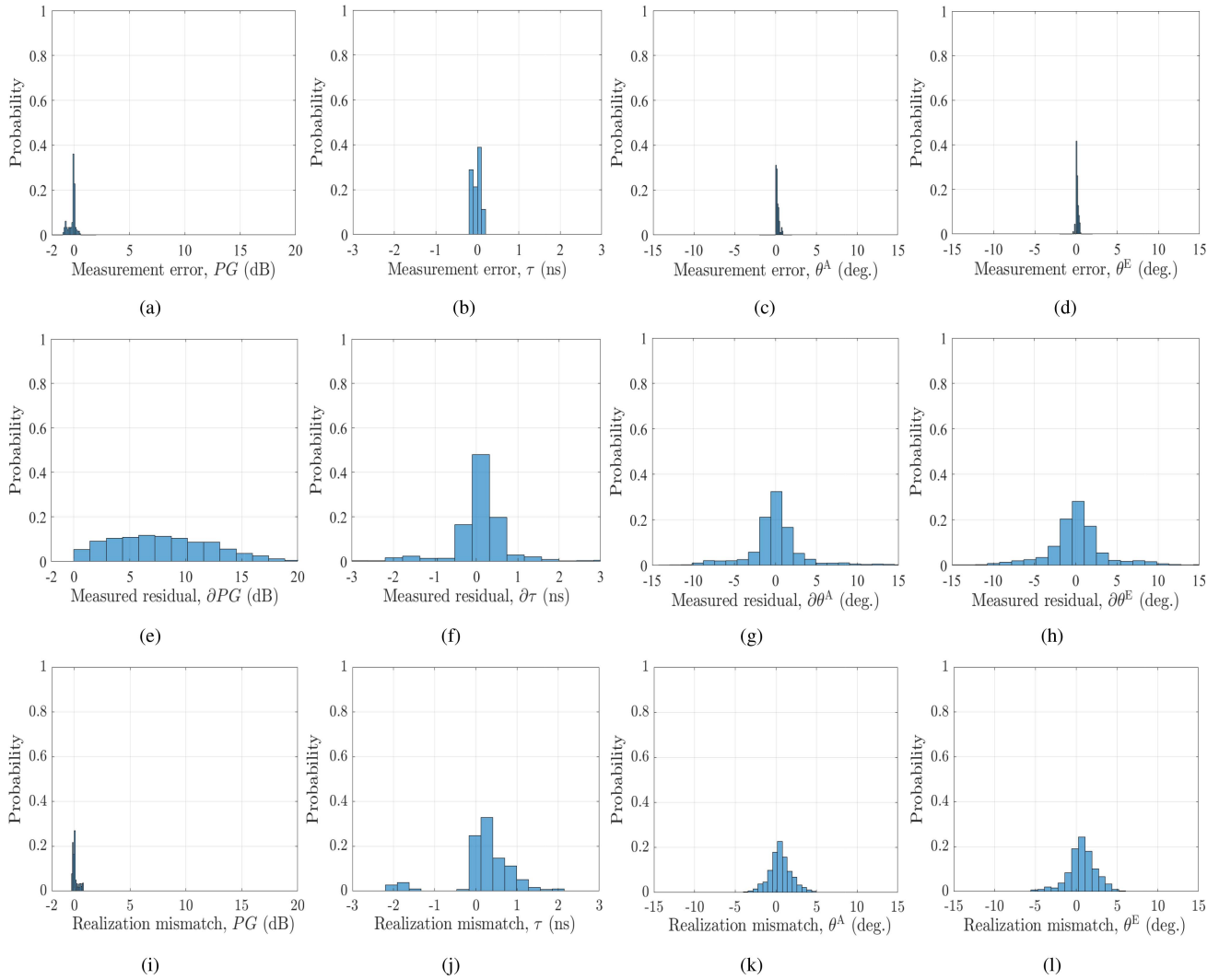
FIGURE 2. Probability density functions in the four domains of the multipath. (a-d) Measurement error of the RF system, aggregated across 90 controlled experiments. (e-h) Measured residual between associated multipaths and keypoints, aggregated across all eight body parts and all times in all 80 cases. (i-l) Realization mismatch between measured and modeled multipath, aggregated across all eight body parts and all times in all 80 cases.

90 rotations are plotted in the first row of Fig. 2(a-d). The absolute average error is only 0.2 dB in path gain (computed from the Friis transmission equation given the measured TX-RX range), 0.1 ns in delay (computed from the speed of light given the measured TX-RX range), and 0.2° in both azimuth and elevation (computed from the rotator angle).

Fig. 3(a) shows the multipaths extracted from a single time acquisition for an illustrative case of Subject A moving their hands from inwards to outwards. Since we are interested in modeling backscatter from the human alone, the multipaths scattered from the environment were filtered in postprocessing by gating the delay and angle to the FoV of the human on the table. Since the table was well isolated from the rest of the environment, the filtering could be implemented reliably. Notice the gated delay from 14 ns to 16.5 ns, equivalent to only 40 cm, the range of the human body, as well as the gated azimuth ($-15°$ to $15°$) and elevation ($-8°$ to $6°$).

2) CAMERA / LIDAR SYSTEMS

The camera and Lidar are used in tandem to extract keypoints from the measurements. The iSTAR Pulsar camera from NCTech[1] captures RGB images at a rate of 7 Hz (every 143 ms). It records the RGB value at each pixel of a 11000×5500 image within the 360° azimuth and 145° elevation FoV synthesized by four fisheye lenses. Simultaneously, the OS0-128 Lidar from Ouster[1] captures range maps at a rate of 10 Hz (every 100 ms). By way of mechanical scanning, it records the range value at each pixel of a 2047×128 map within a 360° azimuth and a 90° elevation FoV.

---

[1]Certain commercial equipment, instruments, or materials are identified in this paper in order to specify the experimental procedure adequately. Such identification is not intended to imply recommendation or endorsement by National Institute of Standards and Technology (NIST), nor is it intended to imply that the materials or equipment identified are necessarily the best available for the purpose.
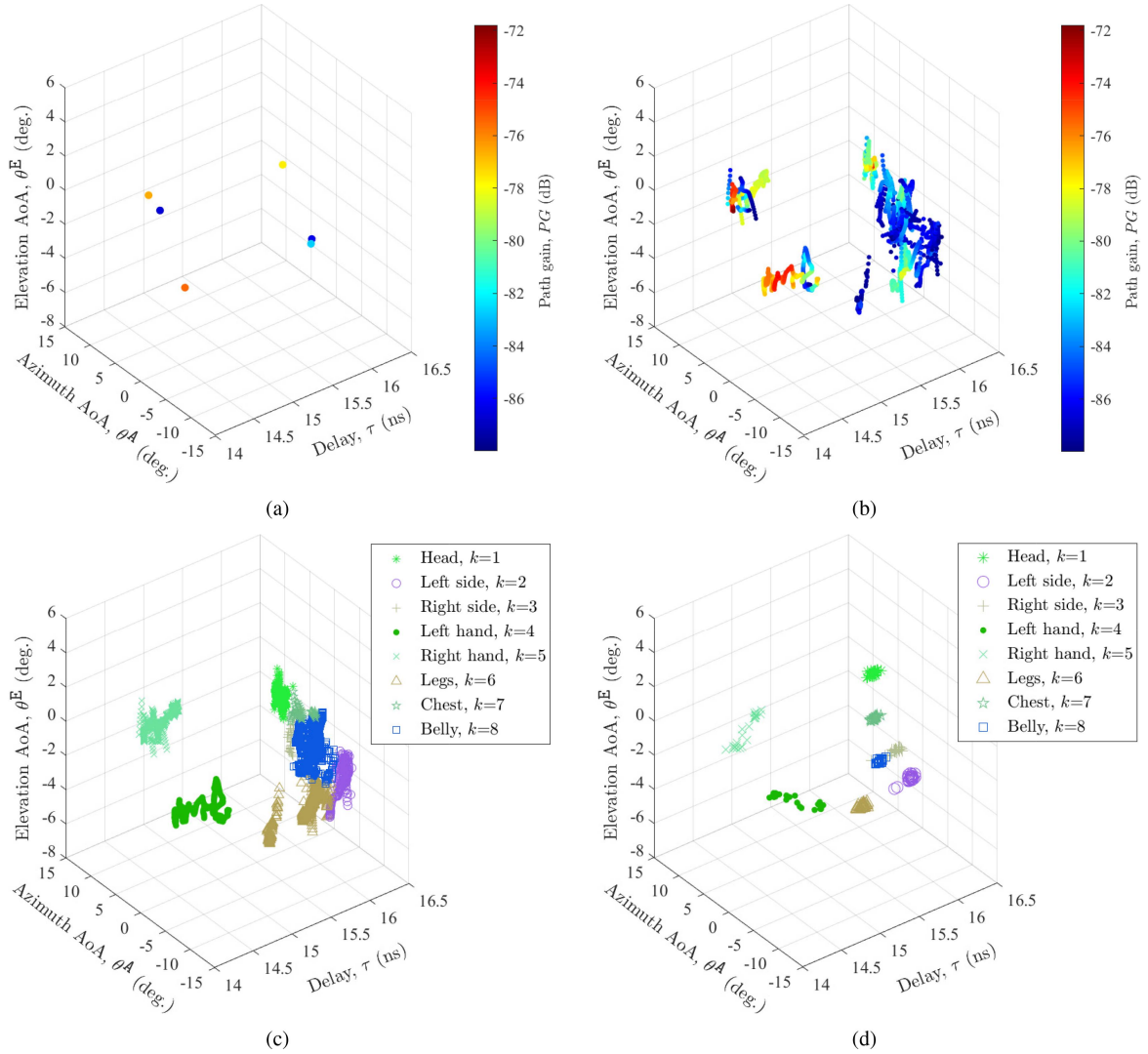
FIGURE 3. (a) Multipaths extracted from a single channel acquisition of an illustrative case. (b) Multipaths extracted from all 1500 channel acquisitions of the illustrative case and aggregated over time. (c) Aggregated multipaths clustered and classified into eight different body parts. (d) Aggregated keypoints clustered and classified into the corresponding eight body parts.

The RGB images recorded by the camera are processed into 17 keypoints – which correspond to the salient parts of the body (nose, eyes, ears, shoulders, elbows, wrists, hips, knees, and ankles) – in azimuth and elevation through the High-Resolution Net (HRNet) algorithm [28]. HRNet is a state-of-the-art artificial intelligence (AI) algorithm that performs repeated multiscale fusions to boost high-resolution representations with help from low-resolution representations, preserving the high-resolution representations throughout the whole process. We use the top-down approach for human-pose estimation, which means that we first detect the bounding boxes of the persons using Faster R-CNN [29], a region-proposal network that shares full-image convolutional features with the detection network, and then estimate the keypoints for each person detected using HRNet. We use the PyTorch version of HRNet [30] for our implementation.

Once the keypoints are extracted from the images, they are "projected" onto the same four domains as the multipaths as follows: Firstly, the extracted keypoints indexed in pixels are converted to degrees (in azimuth and elevation) by scaling the image size to match the 2D FoV of the camera (see Fig. 4(a)). Analogously, the range maps indexed in pixels are converted to degrees (in azimuth and elevation) by scaling the map size to match the 2D FoV of the Lidar. Next, the keypoints are projected onto the range maps (see Fig. 4(b)). That is, the pixel in the map that is closest to the keypoint in the image is isolated, and the range of the keypoint is assigned the range of that closest pixel. Then, the range recorded in meters is converted to delay in nanoseconds by dividing the range by the speed of light (see Fig. 4(c)). Fine temporal synchronization between the three systems is maintained by using the Rubidium clock of the RF system as a reference. Since the three systems have different sample
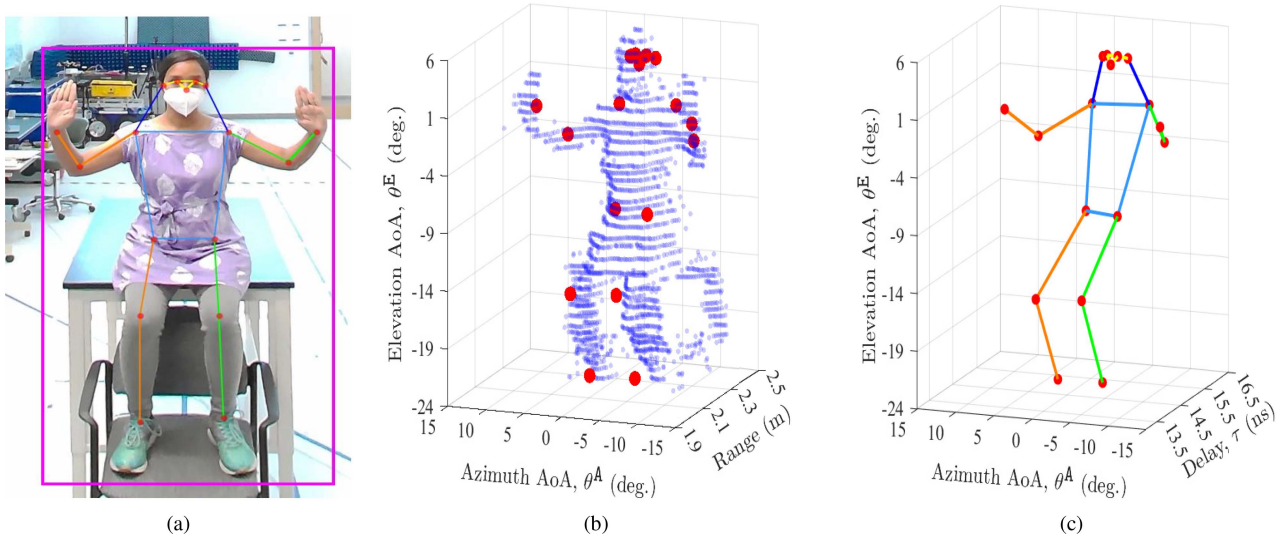
FIGURE 4. Projection of the keypoints into the same domain of the multipaths. (a) Keypoints extracted from the camera images. (b) Extracted keypoints projected onto the Lidar depth maps. (c) Final keypoints projected into the azimuth, elevation, and delay domains.

rates, we used the RF system, which has the highest sample rate, as a reference, and selected the camera and Lidar samples that are closest in time for projection. Finally, keypoint is assigned a path gain that is equivalent to free-space propagation loss, computed from the bistatic Radar equation [31] by setting the Radar cross-section value σ equal to 1.

At the RX end pictured in Fig. 1(c), the camera is mounted directly above the Lidar and the Lidar is mounted directly above the RF antennas to minimize any elevation offset between the three systems while aligning their three sensors as well as possible in azimuth. Fine spatial synchronization between the three systems was then realized by placing control markers in the scene (*e.g.*, metal spheres), which are clearly identifiable in the camera images and Lidar maps and from which a clear reflected path is detected by the RF system. The offsets in the markers between the three systems were measured and calibrated in postprocessing.

III. CHANNEL MODEL
In this section, we describe how the multipaths and keypoints extracted from the measurements were reduced into a channel model. In Section III-A, the multipaths were classified in terms of which body parts backscattered the radiated power into the RX, as a means to associate them to the keypoints. In Section III-B, residuals between the associated multipaths and keypoints were reduced into model parameters. A block diagram of the reduction procedure is shown in Fig. 5(a).

A. MULTIPATH CLASSIFICATION
The first step in classifying the multipaths was to cluster them via our density-based algorithm [32]. While most algorithms cluster multipaths over the path gain, delay, and angle domains only, our algorithm clusters over time as well [20]. This enables multipaths backscattered from

different body parts that are seemingly close *per time* to be discriminated via the tracks they form *over time*. Another benefit of the algorithm is the temporal consistency that is rendered as a byproduct. Consider the illustrative case for Subject A moving their hands inwards to outwards in Fig. 3. While viewing the multipaths per time in Fig. 3(a) provides little clustering information, clusters clearly emerge in Fig. 3(b) when the multipaths are aggregated over time; most notably, two distinct clusters around 15 ns can be associated with the left and right hands, the two clusters that arrive earliest as they are closest to the RX. Fig. 3(c) displays the clustering results for the multipaths: eight clusters indexed as $k = 1, \ldots, 8$ are found.

Although Fig. 3(c) shows the multipaths in both the delay and angle domains, the RF signature of the human body can be more clearly recognized in the angle domains only, shown in Fig. 6(a). During the measurements, accurate records of each case, complete with a diagram, were maintained. See Fig. 6(b) for the diagram corresponding to the illustrative case for Subject A, the shortest of the four subjects. The azimuth wingspans of the hands were recorded for the inwards position ($\theta^A = \pm 4.1°$) and the outwards position ($\theta^A = \pm 9.5°$). It is interesting to note that the multipaths for the hands in Fig. 6(a) extend across almost exactly the same wingspans depicted in Fig. 6(b). What is even more interesting is that for Subject D – the tallest of the four subjects – the multipaths for the hands in Fig. 6(c) also extend across almost exactly the wider wingspans ($\theta^A = \pm 5.8°$ to $\pm 10.7°$) depicted in Fig. 6(d). Indeed, one can view the RF signature of Subject A as a compressed and shifted version of Subject D's: the head at $\theta^E = 2°$ for Subject A vs. $\theta^E = 4°$ for Subject D, the belly at $\theta^E = 2°$ for Subject A vs. $\theta^E = 0°$ for Subject D, etc. This demonstrates that the RF system is capable of capturing the human RF signature with high fidelity.
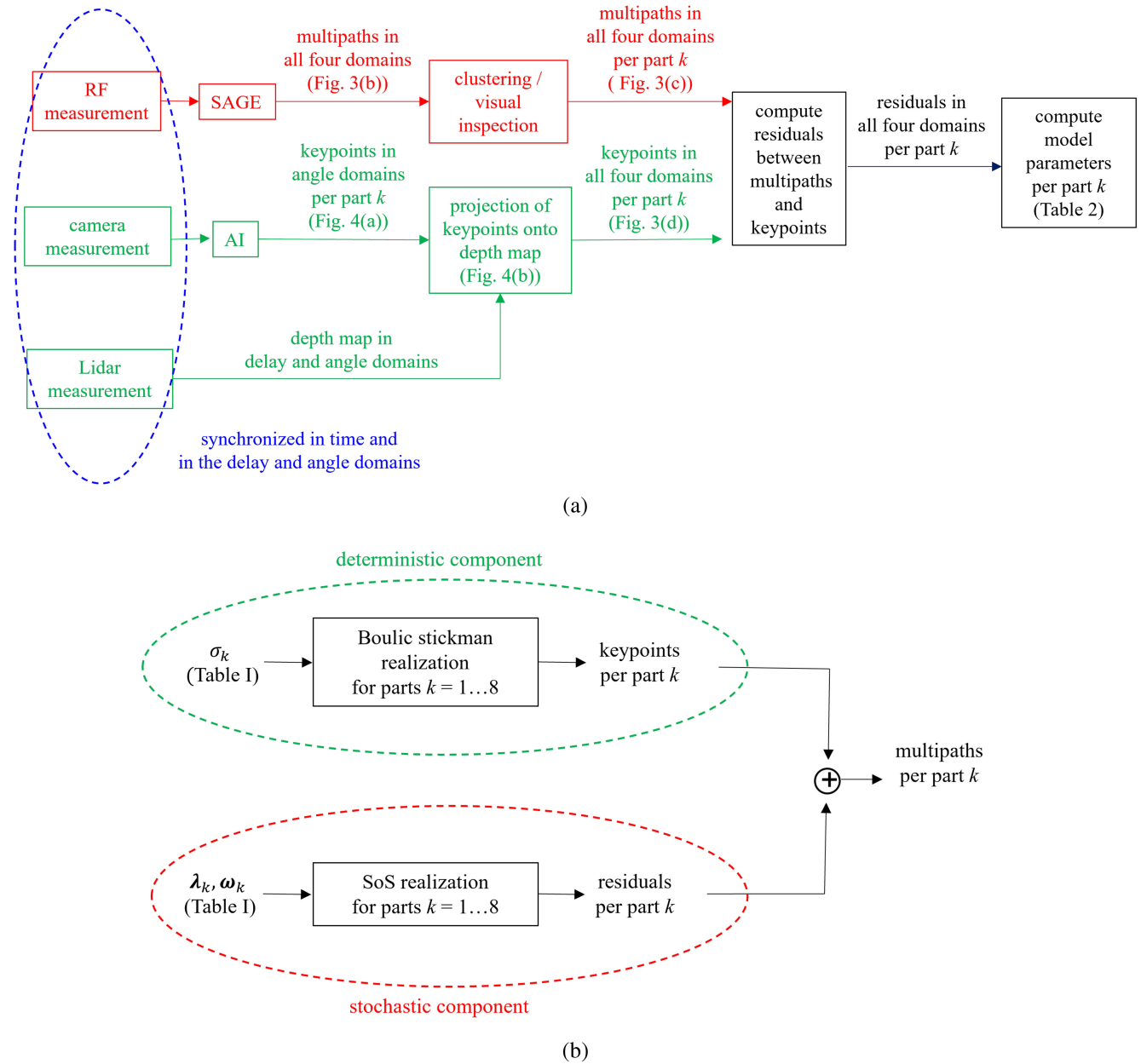
(a)

(b)

FIGURE 5. Block diagrams for the (a) channel model reduction procedure (Section III) and for the (b) channel realization procedure (Section IV).

Next, the keypoints extracted from the camera / Lidar systems were also clustered, but based directly on the classification of the body parts that is given by the keypoint extraction algorithm. Fig. 3(d) displays the clustered keypoints and their classification. The final step was to associate the clustered multipaths to the clustered keypoints by way of visual inspection. But the 17 keypoints correspond to salient body parts, not necessarily to the scatter centers of the multipath... or the RF system simply does not have enough resolution to resolve all the scatter centers. As such, the number of keypoints was reduced from 17 to eight to match the number of multipath clusters, and the keypoints were also shifted such that the cluster centers of the keypoints and the

multipaths were aligned. Specifically, the modified keypoints were computed as polygon centers, polygons delineated by the original keypoints; this ensures that the modified keypoints move in unison with the original keypoints. For example, the modified chest keypoint was calculated as the center of the polygon delineated by the two original shoulder keypoints and the two original hip keypoints. The method described in [33] was implemented to compute the polygon centers. The original and modified keypoints are shown in Fig. 7(a) and 7(b), respectively.

The keypoints can accurately model the gross motion of the body – walking, sitting, hand gesturing, etc. – motion that is deterministic. In that capacity, the keypoints form the
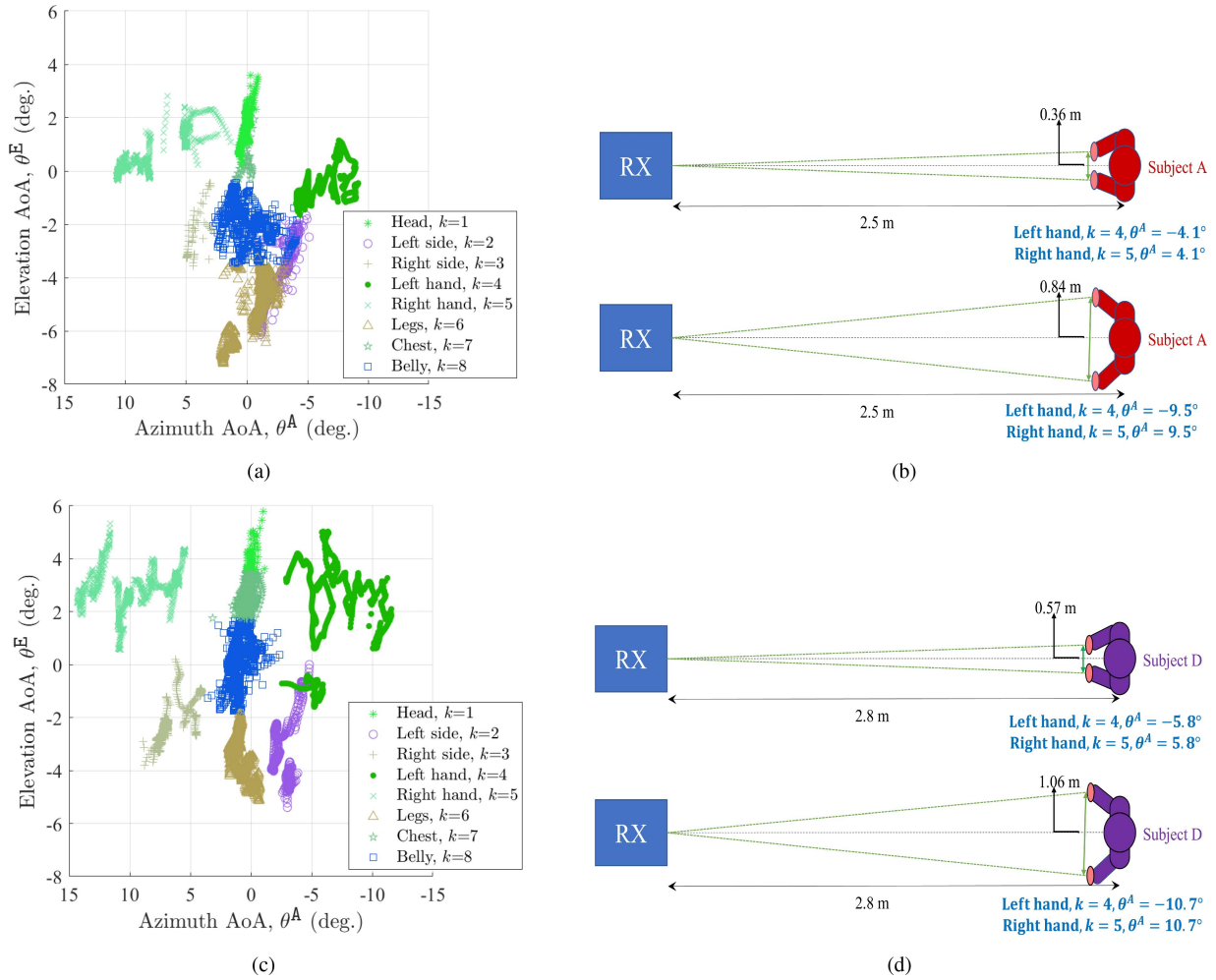
(a)

(b)

(c)

(d)

FIGURE 6. Clustered multipaths in the azimuth and elevation domains for the illustrative case of (a) Subject A and (c) Subject D moving their hands inwards to outwards. Diagrams recorded for the illustrative case during measurement of (b) Subject A and (d) Subject D. The azimuth span of multipaths corresponding to the left and right hands follows those predicted by the wingspan in the diagrams, with wider wingspans for Subject D ($\pm5.8°$ to $\pm10.7°$) with respect to Subject A ($\pm4.1°$ to $\pm9.5°$), as expected from their respective larger and smaller body dimensions.

deterministic component of our QD model. The keypoints, however, represent point scatterers when in reality body parts – non-flat, intricate surfaces – do not behave as point scatterers. For example, depending on the orientation of the hand, it may or may not backscatter radiated power whereas a point scatterer always will. Therefore, the keypoints alone cannot completely characterize the multipath properties. To mitigate their shortcomings, *residuals* between associated multipaths and keypoints are computed and modeled stochastically, as described next.

B. MODEL PARAMETERS

The residual between a pair of associated multipaths and keypoints is computed as their difference in the four domains *per part k* and *per time t*, and is denoted in vector format as $\partial_k(t) = [\partial_{PG_k}(t), \partial_{\tau_k}(t), \partial_{\theta_k^A}(t), \partial_{\theta_k^E}(t)]$. As a byproduct of the multipath clustering, it is possible that more than one multipath (yet seldom more than two) is associated with one keypoint per part and per time. In this situation,
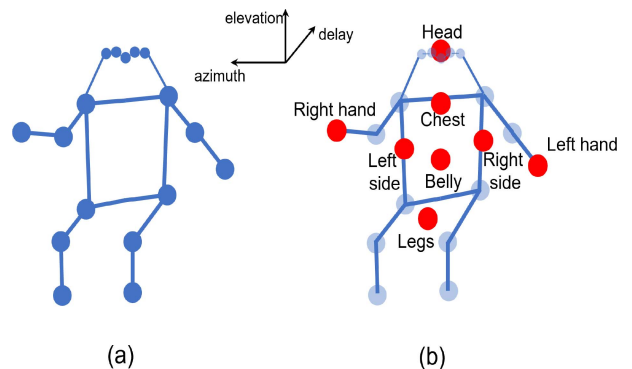
FIGURE 7. (a) Original 17 keypoints extracted from the camera images. (b) Original keypoints (blue) modified from 17 to eight (red), reduced such that the number of keypoints matches the number of multipath clusters and shifted such the cluster centers of the keypoints and the multipaths are aligned.

their composite path gain is computed as the sum over the individual (linear) *PG*s; their composite delay, composite azimuth, and composite elevation are computed as the

TABLE 2. Parameters of the quasi-deterministic channel model for the gesture recognition use case.

Model parameters	Subject	Body parts					
		Head $k = 1$	Left / right side $k = 2 / 3$	Left / right hand $k = 4 / 5$	Legs $k = 6$	Chest $k = 7$	Belly $k = 8$
σ (dB·m^2)	A	-19.17	-23.09	-19.88	-23.80	-19.85	-19.95
	B	-21.32	-17.87	-18.60	-18.85	-19.14	-18.32
	C	-22.88	-19.75	-18.49	-17.37	-20.40	-18.03
	D	-23.23	-16.60	-17.69	-15.46	-22.41	-16.14
$\lambda_{PG}, \omega_{PG}$ (ms^{-1}, ms^{-1})	A	62, 63	134, 147	62, 63	71, 73	94, 99	118, 141
	B	98, 154	149, 152	38, 33	77, 102	101, 110	108, 112
	C	130, 160	117, 130	44, 42	89, 98	110, 109	94, 107
	D	99, 101	160, 180	50, 59	51, 66	123, 139	102, 127
$\lambda_{\tau}, \omega_{\tau}$ (ms^{-1}, ms^{-1})	A	132, 139	136, 145	52, 51	98, 71	119, 122	110, 130
	B	110, 139	156, 176	58, 49	90, 111	131, 139	114, 149
	C	147, 176	117, 139	55, 52	113, 148	142, 152	106, 106
	D	130, 150	140, 191	68, 78	120, 160	152, 179	99, 133
$\lambda_{\theta A}, \omega_{\theta A}$ (ms^{-1}, ms^{-1})	A	85, 86	127, 141	52, 58	110, 112	113, 130	131, 149
	B	116, 152	96, 121	53, 39	97, 78	145, 145	123, 133
	C	113, 155	120, 125	65, 44	73, 115	129, 121	137, 150
	D	117, 143	157, 169	62, 65	53, 81	143, 155	124, 133
$\lambda_{\theta E}, \omega_{\theta E}$ (ms^{-1}, ms^{-1})	A	68, 91	132, 149	66, 70	101, 98	123, 139	118, 146
	B	104, 134	102, 130	52, 40	87, 90	133, 154	134, 140
	C	107, 146	135, 145	65, 55	76, 99	133, 164	95, 136
	D	115, 133	131, 181	55, 58	60, 80	149, 166	95, 120

weighted root-mean-square value, weighted by the individual *PG*s. Fig. 2(e-h) shows the distribution of the residual in the four domains aggregated over all parts and all times in all cases. It is interesting to compare the residual distributions to the measurement error distributions in Fig. 2(a-d) per domain. It is obvious that the residual distributions are much wider than the measurement error distributions, indicating that the residual captures actual scattering properties of the channel, not measurement error.

The distributions for the residual delay, residual azimuth, and residual elevation are all centered around zero, and so are modeled accordingly – that is – with zero offset between the keypoints and the multipaths. However, there is an obvious non-zero offset in the residual path gain. Recall from Section II-B.2 that the keypoint is assigned a path gain that is equivalent to free-space propagation loss. The path gain of the multipath, however, in addition to free-space propagation loss, also includes the Radar cross-section value, which is the backscatter loss from the body. So the non-zero offset in the path gain residual is effectively the σ value. As the first parameter in our model, we report the average σ per part in Table 2, averaged over all times in all cases. Due to the symmetry of the body, the hands and sides of the body are combined into a single parameter respectively.

With the residual offsets accounted for in the model, we now turn our focus to how the residual spreads are modeled. A simple modeling approach is to empirically fit parametric distributions to Fig. 2(e-h) and, when generating channel realizations, draw random trials from each per time. The

underlying assumption is that realizations are temporally uncorrelated; however, as we shall see next, their temporal correlation can in fact be significant. To substantiate this, we calculate the autocorrelation function (ACF) over time of the kth residual per domain [·] as:

$$\boldsymbol{R}_{[\cdot]_k}(\Delta t) = \frac{\sum_t \partial_{[\cdot]_k}(t)\partial_{[\cdot]_k}(t + \Delta t)}{\sum_t \partial^2_{[\cdot]_k}(t)}. \quad (1)$$

The ACF is assumed to be wide-sense stationary [34] – that is – the correlation between any time t and some later time $t + \Delta t$ depends only on the time difference Δt and not on the absolute time t. That is why the ACF can be computed in Eq. (1) by averaging over all absolute times. By virtue of the normalizing factor in the denominator, an ACF value of 1 represents perfect correlation, -1 perfect negative correlation, and 0 represents no correlation at all. As an example, Fig. 8 shows the measured ACF (blue line) in the elevation domain for the right hand ($k = 3$) of Subject A in the illustrative case.

The ACFs exhibit damped sinusoid behavior – this was consistent across all ACFs calculated in all domains and across all parts and subjects. This behavior was also observed in [35], [36] when modeling temporal consistency. In [36], the following expression[2] to model this behavior is proposed:

$$\hat{\boldsymbol{R}}_{[\cdot]_k}(\Delta t) = e^{-\lambda_{[\cdot]_k}\Delta t}\cos\big(\boldsymbol{\omega}_{[\cdot]_k}\Delta t\big), \quad (2)$$

[2]Our expression is a numerically stable version of the expression for the damped sinusoid in [36].
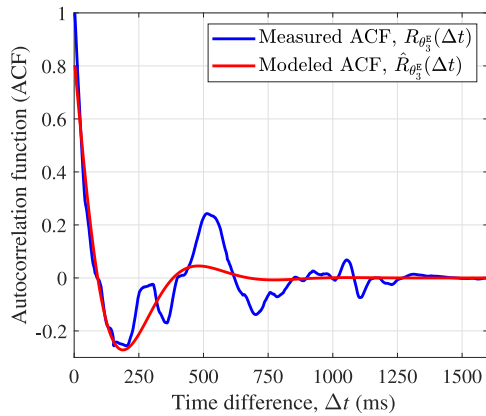
FIGURE 8. Modeled ACF versus measured ACF for EL domain of the right hand of Subject A in the illustrative case.

where the parameter λ denotes the decay constant and ω denotes the angular frequency of the sinusoid. The smaller the decay constant, the longer the correlation time, defined as the time at which the ACF first dips below $1/e = 0.37$. When $\lambda < \omega$, the ACF is considered underdamped and is otherwise considered overdamped. In the former case, oscillatory behavior (as seen in the ACFs in Fig. 8) is present, for which the ACF drops below zero; in the latter case, the ACF never drops below zero and rather decays only.

To capture the temporal correlation of the residuals, the parameters of the model ACF in Eq. (2) were fit to the measured ACFs in Eq. (1), individually for all parts and for all subjects in all cases. Fig. 8 shows the modeled ACF (red) fit to the measured ACF (blue). We see that the damped sinusoid model provides a good approximation of the observed behavior, particularly at the start of the ACF. Of particular importance is the accuracy in which the oscillatory behavior (where the ACF drops below zero) is modeled. The fitted model parameters were then averaged across the cases, and reported in Table 2.

When analyzing the σ parameter, we note the observable trend of a larger RCS value for the taller subjects across body parts, indicating larger losses (as values are negative a larger value is represented by a lower number). This likely stems from the increased surface area of the body parts with the taller subjects. Similarly, the chest, the largest body part by surface area, exhibits the largest RCS values, whereas the hands and head exhibit the smallest RCS values. This trend is observed across all four subjects.

When analyzing the λ parameter of the damped sinusoid model, it is evident across all four subjects that the hands have longer correlation time than the other parts of the body (smaller λ corresponds to longer correlation time). This is because their multipaths can be clearly discriminated thanks to their shorter delays (they are removed from the rest of the body) and to their motion. As such, they can be reliably clustered. In contrast, the other body parts have similar delay and are static, so their multipaths can be discriminated in

angle alone, leading to clusters that combine multipath across larger scattering areas of the body. The combination of more multipath in the clusters translates to shorter correlation time. This is most evident for the chest and the sides, whose clusters are the largest (see Fig. 6). The head, rather, even though static, is also somewhat removed from the rest of the body – as are the hands – and therefore also features longer correlation times.

Another noticeable trend is longer correlation times of the path gain compared to delay, azimuth, and elevation, meaning that it does not fluctuate as rapidly as the other geometrical parameters. When considering differences in parameters between subjects, it is noticeable that for the hands, sides, head and chest, the shortest subject (Subject A) displays greater correlation than the tallest subject (Subject D). In general, this trend is also present in the parameters for Subject B and Subject C. Similarly to the discussion above, the increased surface area of the body parts for the taller subjects leads to a wider dispersion of multipaths. This in turn can cause the geometrical cluster centroid to fluctuate significantly with time, resulting in the correlation decaying rapidly.

IV. CHANNEL REALIZATION
As the proposed model represents humans only, a complete channel realization requires a complementary model (*e.g.*, [6], [19], [20], [21]) to represent the environment surrounding the humans; the multipaths from the environment are then combined with the multipaths from the human (or multiple humans) realized. In this section, we simply describe how channel realizations for a single human are generated from the model: In Section IV-A, we describe how the deterministic component of the realizations is generated, followed by a description of the stochastic component in Section IV-B. A block diagram of the channel realization procedure is shown in Fig. 5(b). In the Section IV-C, the model is validated by comparing the realizations against the measurements.

A. DETERMINISTIC COMPONENT
As keypoints were used to reduce a channel model from the measurements, they are in kind used to generate realizations of the channel from the model; except that in the former case keypoints were extracted from the camera/Lidar systems while in the latter case keypoints are generated from the Boulic stickman [37], a collection of keypoints that delineate the body. But in addition to simply delineating the body, the keypoints of the Boulic stickman are temporally correlated so that they move in unison to mimic human gait, provided the trajectory of the body (defined by the position of a single reference keypoint over time), the limb speed, and the dimensions of the body (height, width, and depth). The Boulic stickman is most suitable for generating realizations of the walking use case for human sensing that we consider in other work [11], [38]. For the gesture recognition use case that we consider here, the original stickman was modified

to allow the hands to move independently – each hand within the sphere circumscribed by the maximum extension of the arm – while maintaining correlation between the other keypoints. And, consistent with Section III-A, the keypoints in the original stickman were interpolated to correspond to the eight body parts modeled in this work.

The first step in generating a channel realization is to generate a realization of the modified Boulic stickman for a subject of interest, scaled to their body dimensions. The realization of the stickman is expressed as a time series, analogous to the time series of the 1500 channel acquisitions in a measurement. Then, at each time in the series, a ray is traced from the TX to the kth keypoint and back to the RX, yielding the modeled keypoint delay $\hat{\tau}_k(t)$, azimuth AoA $\hat{\theta}_k^{\text{A}}(t)$, and elevation AoA $\hat{\theta}_k^{\text{E}}(t)$. The delay and AoA are converted to the bistatic free-space path gain and the appropriate σ parameter from Table 2 is added, yielding the modeled keypoint path gain $\hat{PG}_k(t)$.

B. STOCHASTIC COMPONENT

To the deterministic component of the model $[\hat{PG}_k(t), \hat{\tau}_k(t), \hat{\theta}_k^{\text{A}}(t), \hat{\theta}_k^{\text{E}}(t)]$, a counterpart stochastic component $\hat{\partial}_{[\cdot]_k}(t)$ characterizing the modeled residual is added, completing the channel realization. The modeled residual is generated independently in each of the four domains through the SoS process [39], [40]. By way of this process, the modeled residual can be generated such that its ACF can approximate any arbitrary ACF, as described next.

The modeled residual is represented as a sum of N sinusoids:

$$\hat{\partial}_{[\cdot]_k}(t) = \sum_{n=1}^{N} a_{[\cdot]_k}^n \cos\left(2\pi f_{[\cdot]_k}^n t + \psi^n\right). \quad (3)$$

The values for the amplitudes a^n and the frequencies f^n are found through a Monte-Carlo technique [39], effectively by iteratively matching the ACF of $\hat{\partial}_{[\cdot]_k}(t)$ to the ACF in Eq. (2) (defined by the appropriate parameters λ and ω from Table 2) until a certain error threshold is reached. We found that $N = 50$ sinusoids was sufficient to reach the desired threshold. Note that for each domain $[\cdot]$ and for each part k, $a_{[\cdot]_k}^n$ and $f_{[\cdot]_k}^n$ must be calculated independently whereas $\psi^n \sim \mathcal{U}[-\pi, \pi]$. A key feature of the SoS process is that by keeping the a^n and f^n fixed but resampling ψ^n, a different realization of the residuals will be generated while still approximating the same ACF. For example, for one realization the residual may increase initially but for a second realization, it may decrease. Finally, we set the residuals at time $t = 0$ in the series to zero ($\hat{\partial}_k(0) = 0$) such that the channel at the first time is completely defined by the deterministic component.

Once generated, the deterministic and stochastic realizations are combined into the following directional channel impulse response:

$$\hat{h}\left(t, \tau, \theta^{\text{A}}, \theta^{\text{E}}\right) = \sum_{k=1}^{8} \sqrt{\hat{PG}_k(t) + \hat{\partial}_{PG_k}(t)}$$

$$\cdot e^{j\left[2\pi f_{\text{c}}\left[t - \hat{\tau}_k(t) - \hat{\partial}_{\tau_k}(t)\right] + \psi_k\right]}$$

$$\cdot \delta\left[\tau - \hat{\tau}_k(t) - \hat{\partial}_{\tau_k}(t), \theta^{\text{A}} - \hat{\theta}_k^{\text{A}}(t) - \hat{\partial}_{\theta_k^{\text{A}}}(t),\right.$$

$$\left. \theta^{\text{E}} - \hat{\theta}_k^{\text{E}}(t) - \hat{\partial}_{\theta_k^{\text{E}}}(t)\right], \quad (4)$$

where f_{c} is the center frequency, $\psi_k \sim \mathcal{U}[-\pi, \pi]$ is a random phase, and and δ is the Dirac delta function. Although the response is only single directional, the double-directional response $\hat{h}(t, \tau, \theta^{\text{A}}, \theta^{\text{E}}, \theta^{\text{TX,A}}, \theta^{\text{TX,E}})$ – augmented to include azimuth and elevation AoD denoted as $\theta^{\text{TX,A}}$ and $\theta^{\text{TX,E}}$ respectively – follows directly from Eq. (4) since each multipath k originates from a single bounce. That means that – as for our RF system that only estimates AoA (not AoD) – its AoD can be computed uniquely in terms of its delay $\hat{\tau}_k(t) + \hat{\partial}_{\tau_k}(t)$, azimuth AoA $\hat{\theta}_k^{\text{A}}(t) + \hat{\partial}_{\theta_k^{\text{A}}}(t)$, and elevation AoA $\hat{\theta}_k^{\text{E}}(t) + \hat{\partial}_{\theta_k^{\text{E}}}(t)$. Details of the computation are provided in [25].

The channel impulse response in Eq. (4) only considers the eight parts in the measurements that were both resolvable (given the finite beamwidth and bandwidth of the RF system) and detectable (given its finite FoV and link budget). However, others parts can be included in the model – *i.e.*, the feet, which went undetected – by substituting the parameters in Table 2 of the parts that are most similar. Care should be taken so that the 3D separation in the delay / angle domains between all parts included is maintained (see Fig. 7(b)). That is because, as explained in Section III-B, the path gain of any part can be the composite over several multipaths from the same cluster, so the 3D separation between the cluster centroids is implicit to the parameters in the table.

C. VALIDATION

We validate the channel model by comparing the multipaths generated by the model to the multipaths measured by the channel sounder. As an example, Fig. 9 shows the multipaths in each of the four domains for Subject A's right hand in the illustrative case. Specifically, each plot shows the modeled keypoint, the modeled residual (a single SoS realization), the modeled multipath (obtained by adding the modeled residual to the modeled keypoint), and the corresponding measured multipath. Fig. 9(c) clearly shows that the right hand moves predominantly in the azimuth domain (hand moves from inwards to outwards), with the azimuth angle of the deterministic component decreasing by about 4° throughout the entire gesture. The Boulic stickman provides an accurate approximation of the general motion of the hand by way of the deterministic modeled keypoints, albeit in a linear fashion. When the stochastic modeled residual component is added, the combined modeled multipath closely matches the measured multipath. Similarly, in Fig. 9(a,b) the simulated realization provides a very accurate approximation of the measured multipath. In Fig. 9(d), significantly more fluctuation is visible in the elevation domain of the measured multipath. This is well reflected in the generated residual, which has a shorter correlation time (hence more fluctuation) as specified by the parameters in Table 2.
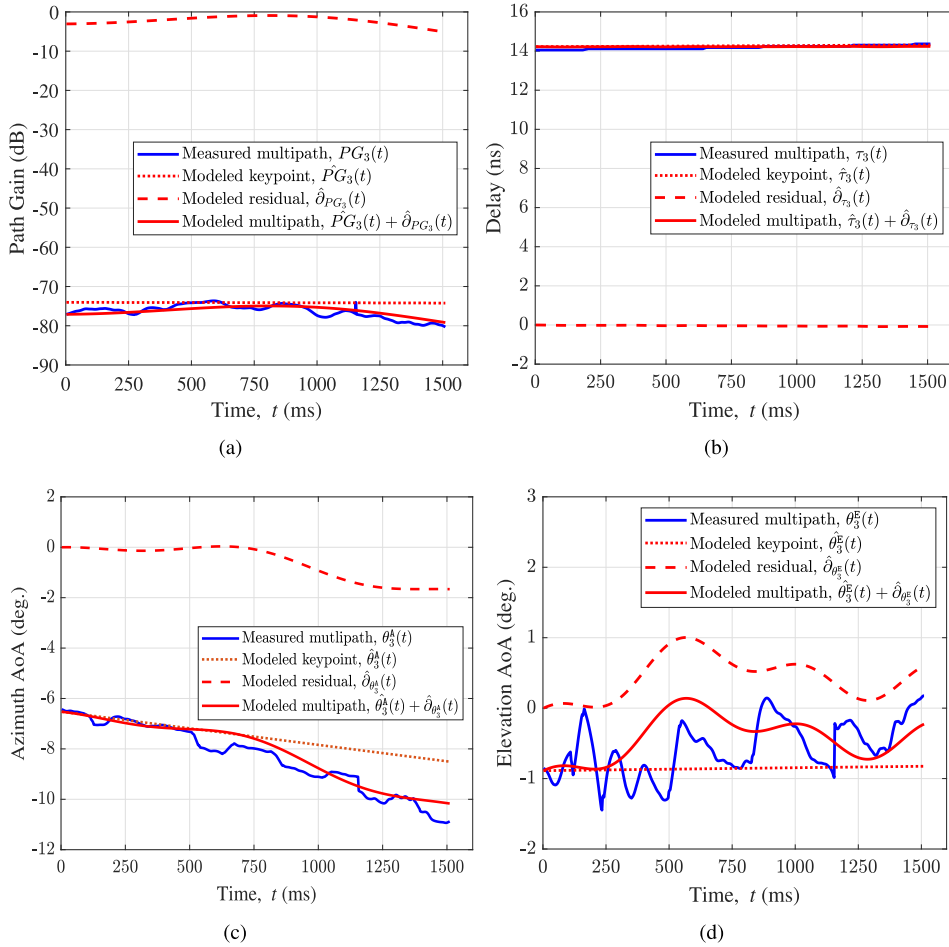
FIGURE 9. Example of overall realization generation using illustrative example. (a) Path Gain. (b) Delay. (c) Azimuth. (d) Elevation.

For comprehensive model validation, realizations of the channel were generated from the model parameters in Table 2 to emulate all 80 measured cases. At each time, the mismatch between the modeled multipath and the measured multipath was computed per domain partwise. This was repeated for 100 different SoS processes. Finally, the realization mismatches were aggregated across all times in all 80 cases across all 100 SoS processes per case, into the four probability density functions (PDFs) in Fig. 2(i-l) per domain.

Across all four domains, we see the largest probabilities are centered around zero, indicating good agreement between the realizations and the measurements. Of note is the narrow spread of the path gain and delay mismatches compared to the other domains. For the path gain mismatch, 100% of the mismatches are between −1 dB and 1 dB; similarly, 90% of the delay domain mismatches are between −1 ns and 1 ns. This indicates that the two domains are particularly well approximated by the model. Despite the greater spread, the angular domains still showed good agreement with the model, with 85% and 70% of mismatches between −2 and 2 (deg.) for the azimuth and elevation domains respectively. When comparing the realization mismatches to

the measured residuals in the previous row, we note the maximum errors are significantly less than the maximum residuals. This shows that the addition of the stochastic component (the modeled residual) significantly improves the performance of the model in comparison to the use of a deterministic component only. Furthermore, it can be observed that the realization mismatches in Fig. 2(i-l) have a similar distribution shape to the residuals in Fig. 2(e-h), albeit the range of values is significantly lower.

V. CONCLUSION

In this paper, we describe a methodology to reduce the high-resolution measurements that were collected with our 28 GHz context-aware channel sounder to a quasi-deterministic channel propagation model for human sensing, considering gesture recognition as the use case. The deterministic component of the model is realized by way of the Boulic stickman, to represent the human body and capture the temporal consistency that is required for sensing applications. The stochastic component of the model is realized by way of the Sum-of-Sinusoid process, to capture the non-specular nature of backscatter from the human body, reconciling the simplicity of the Boulic stickman with the

accuracy of the measurements. The stochastic parameters found differed between body parts and across the four human subjects, however with identifiable and consistent trends.

To demonstrate the accuracy of the model, a comprehensive validation was conducted: Across all body parts and subjects, multipaths were generated using the model for each of the 20 distinct body motions. The mismatch between these multipaths and the corresponding measured multipaths was calculated. Across all four domains, the distribution of the mismatches are centered around zero, indicating excellent agreement between the model and measurements. Critically, these mismatches are much smaller than the residuals calculated from measurements, indicating that the introduction of the stochastic component significantly increases accuracy.

REFERENCES

[1] J. Wang, N. Varshney, C. Gentile, S. Blandino, J. Chuang, and N. Golmie, "Integrated sensing and communication: Enabling techniques, applications, tools and data sets, standardization, and future directions," *IEEE Internet Things J.*, vol. 9, no. 23, pp. 23416–23440, Dec. 2022.

[2] N. Y. Philip, J. J. P. C. Rodrigues, H. Wang, S. J. Fong, and J. Chen, "Internet of Things for in-home health monitoring systems: Current advances, challenges and future directions," *IEEE J. Sel. Areas Commun.*, vol. 39, no. 2, pp. 300–310, Feb. 2021.

[3] H. Xu, W. Yu, D. Griffith, and N. Golmie, "A survey on Industrial Internet of Things: A cyber-physical systems perspective," *IEEE Access*, vol. 6, pp. 78238–78259, 2018.

[4] Y. A. Qadri, A. Nauman, Y. B. Zikria, A. V. Vasilakos, and S. W. Kim, "The future of healthcare Internet of Things: A survey of emerging technologies," *IEEE Commun. Surveys Tuts.*, vol. 22, no. 2, pp. 1121–1167, 2nd Quart., 2020.

[5] A. Haydari and Y. Yılmaz, "Deep reinforcement learning for intelligent transportation systems: A survey," *IEEE Trans. Intell. Transp. Syst.*, vol. 23, no. 1, pp. 11–32, Jan. 2022.

[6] Q. Zhu, C.-X. Wang, B. Hua, K. Mao, S. Jiang, and M. Yao, *3GPP TR 9997537901 Channel Model*. Hoboken, NJ, USA: Wiley, 2021, pp. 1–35. [Online]. Available: https://onlinelibrary.wiley.com/doi/abs/10.1002/9781119471509.w5GRef048

[7] Y. Xing and T. S. Rappaport, "Propagation measurement system and approach at 140 GHz-moving to 6G and above 100 GHz," in *Proc. IEEE Global Commun. Conf. (GLOBECOM)*, 2018, pp. 1–6.

[8] H. Tataria, M. Shafi, A. F. Molisch, M. Dohler, H. Sjöland, and F. Tufvesson, "6G wireless systems: Vision, requirements, challenges, insights, and opportunities," *Proc. IEEE*, vol. 109, no. 7, pp. 1166–1199, Jul. 2021.

[9] M. Vahidpour and K. Sarabandi, "Millimeter wave RCS and doppler spectrum of walking human and dog," in *Proc. IEEE Antennas Propag. Soc. Int. Symp.*, 2007, pp. 4004–4007.

[10] S. Mukherjee, G. Skidmore, T. Chawla, A. Bhardwaj, C. Gentile, and J. Senic, "Scalable modeling of human blockage at millimeter-wave: A comparative analysis of knife-edge diffraction, the uniform theory of diffraction, and physical optics against 60 GHz channel measurements," *IEEE Access*, vol. 10, pp. 133643–133654, 2022.

[11] S. Blandino, T. Ropitault, A. Sahoo, and N. Golmie, "Tools, models and dataset for IEEE 802.11ay CSI-based sensing," in *Proc. IEEE Wireless Commun. Netw. Conf. (WCNC)*, 2022, pp. 662–667.

[12] B. Erol, C. Karabacak, S. Z. Gürbüz, and A. C. Gürbüz, "Simulation of human micro-Doppler signatures with kinect sensor," in *Proc. IEEE Radar Conf.*, 2014, pp. 863–868.

[13] B. Erol and S. Z. Gurbuz, "A kinect-based human micro-Doppler simulator," *IEEE Aerosp. Electron. Syst. Mag.*, vol. 30, no. 5, pp. 6–17, May 2015.

[14] S. S. Ram, C. Christianson, Y. Kim, and H. Ling, "Simulation and analysis of human micro-dopplers in through-wall environments," *IEEE Trans. Geosci. Remote Sens.*, vol. 48, no. 4, pp. 2015–2023, Apr. 2010.

[15] S. S. Ram and H. Ling, "Simulation of human micro dopplers using computer animation data," in *Proc. IEEE Radar Conf.*, 2008, pp. 1–6.

[16] G. Li, S. Wang, J. Li, R. Wang, X. Peng, and T. X. Han, "Wireless sensing with deep spectrogram network and primitive based autoregressive hybrid channel model," in *Proc. IEEE 22nd Int. Workshop Signal Process. Adv. Wireless Commun. (SPAWC)*, 2021, pp. 481–485.

[17] *Part 11: Wireless LAN Medium Access Control (MAC) and Physical Layer (PHY) Specifications–Amendment 2: Enhancements for Wireless LAN Sensing*, IEEE Standard P802.11bf/D0.5, 2022.

[18] "Study on integrated sensing and communication," 3GPP, Sophia Antipolis, France, 3GPP Rep. 22.837, 2023. [Online]. Available: https://www.3gpp.org/DynaReport/22837.htm

[19] A. Maltsev et al., "Quasi-deterministic approach to mmWave channel modeling in a non-stationary environment," in *Proc. IEEE Globecom Workshops (GC Wkshps)*, 2014, pp. 966–971.

[20] N. Varshney, J. Wang, C. Lai, C. Gentile, R. Charbonnier, and Y. Corre, "Quasi-deterministic channel propagation model for an urban environment at 28 GHz," *IEEE Antennas Wireless Propag. Lett.*, vol. 20, no. 7, pp. 1145–1149, Jul. 2021.

[21] J. Yang et al., "Quasi-deterministic modeling for Industrial IoT channels based on millimeter wave measurements," *IEEE Internet Things J.*, vol. 11, no. 5, pp. 8373–8385, Mar. 2024.

[22] A. Bhardwaj, D. Caudill, C. Gentile, J. Chuang, J. Senic, and D. G. Michelson, "Geometrical-empirical channel propagation model for human presence at 60 GHz," *IEEE Access*, vol. 9, pp. 38467–38478, 2021.

[23] A. Nafe, M. Sayginer, K. Kibaroglu, and G. M. Rebeiz, "2x64 dual-polarized dual-beam single-aperture 28 GHz phased array with high cross-polarization rejection for 5G polarization MIMO," in *Proc. IEEE MTT-S Int. Microw. Symp. (IMS)*, 2019, pp. 484–487.

[24] D. Caudill, J. Chuang, S. Y. Jun, C. Gentile, and N. Golmie, "Real-time mmWave channel sounding through switched beamforming with 3-D dual-polarized phased-array antennas," *IEEE Trans. Microw. Theory Techn.*, vol. 69, no. 11, pp. 5021–5032, Nov. 2021.

[25] W. G. Newhall and J. H. Reed, "A geometric air-to-ground radio channel model," in *Proc. MILCOM*, vol. 1, 2002, pp. 632–636.

[26] D. Caudill, J. Chuang, C. Gentile, and S. Y. Jun, "On predistorion filtering for switched beamforming with phased-array antennas," in *Proc. Eur. Conf. Antennas Propag.*, 2023, pp. 1–5.

[27] P. B. Papazian et al., "Calibration of millimeter-wave channel sounders for super-resolution multipath component extraction," in *Proc. 10th Eur. Conf. Antennas Propag. (EuCAP)*, 2016, pp. 1–5.

[28] K. Sun, B. Xiao, D. Liu, and J. Wang, "Deep high-resolution representation learning for human pose estimation," in *Proc. IEEE/CVF Conf. Comput. Vis. Pattern Recognit.*, 2019, pp. 5693–5703.

[29] S. Ren, K. He, R. Girshick, and J. Sun, "Faster R-CNN: Towards real-time object detection with region proposal networks," in *Proc. Adv. Neural Inf. Process. Syst.*, 2015, pp. 91–99.

[30] L. Xiao, H. Wang, M. Heimann, I. Khvedchenia, and R. Stiefelhagen. "Deep high resolution net pytorch." Github.com. 2020. [Online]. Available: https://github.com/leoxiaobin/deep-high-resolution-net.pytorch

[31] B. Radar, *Bistatic Radar: Emerging Technology*. Hoboken, NJ, USA: Wiley, 2008.

[32] J. Wang, C. Gentile, J. Senic, R. Sun, P. B. Papazian, and C. Lai, "Unsupervised clustering for millimeter-wave channel propagation modeling," in *Proc. IEEE 86th Veh. Technol. Conf. (VTC-Fall)*, 2017, pp. 1–4.

[33] G. Bashein and P. R. Detmer, *Centroid of a Polygon*. New York, NY, USA: Academic, 1994, pp. 3–6.

[34] P. Bello, "Characterization of randomly time-variant linear channels," *IEEE Trans. Commun. Syst.*, vol. 11, no. 4, pp. 360–393, Dec. 1963.

[35] S. Ju and T. S. Rappaport, "140 GHz urban microcell propagation measurements for spatial consistency modeling," in *Proc. IEEE Int. Conf. Commun.*, 2021, pp. 1–6.

[36] Y. Zhang, J. Zhang, D. Dong, X. Nie, G. Liu, and P. Zhang, "A novel spatial autocorrelation model of shadow fading in urban macro environments," in *Proc. IEEE Global Commun. Conf. (GLOBECOM)*, 2008, pp. 1–5.

[37] R. Boulic, N. M. Thalmann, and D. Thalmann, "A global human walking model with real-time kinematic personification," *Vis. Comput.*, vol. 6, pp. 344–358, Nov. 1990.

[38] S. Blandino, T. Ropitault, C. R. da Silva, A. Sahoo, and N. Golmie, "IEEE 802.11bf DMG sensing: Enabling high-resolution mmWave Wi-Fi sensing," *IEEE Open J. Veh. Technol.*, vol. 4, pp. 342–355, 2023.

[39] S. Jaeckel, L. Raschkowski, F. Burkhardt, and L. Thiele, "Efficient sum-of-sinusoids-based spatial consistency for the 3GPP new-radio channel model," in *Proc. IEEE Globecom Workshops (GC Wkshps)*, 2018, pp. 1–7.

[40] M. Patzold, U. Killat, and F. Laue, "A deterministic digital simulation model for Suzuki processes with application to a shadowed rayleigh land mobile radio channel," *IEEE Trans. Veh. Technol.*, vol. 45, no. 2, pp. 318–331, May 1996.

NEERAJ VARSHNEY (Senior Member, IEEE) received the B.Tech. degree in electronics and communication engineering from Uttar Pradesh Technical University, Lucknow, India, in 2008, the M.Tech. degree in electronics and communication engineering from the Jaypee Institute of Information Technology, Noida, India, in 2011, and the Ph.D. degree in electrical engineering from the Indian Institute of Technology Kanpur, India, in 2018. Since January 2023, he has been working with the Radio Access and Propagation Metrology Group, National Institute of Standards and Technology, and also associated with Prometheus Computing LLC as a Research Scientist. From October 2011 to August 2012, he was a Project Research Fellow with the Jaypee Institute of Information Technology. From May 2018 to September 2018, he was a Visiting Researcher with the Department of Electrical Engineering and Computer Science, Syracuse University, New York, USA. From November 2018 to December 2022, he was an International Research Associate with the Wireless Networks Division, National Institute of Standards and Technology, Maryland, USA. His research interests are in signal processing, communications, and networks which include mmWave and THz wireless communication, MIMO technology, and molecular communication. Since 2019, he has been serving as a TPC Member for IEEE Globecom conferences in the track of Molecular, Biological, and Multi-Scale Communications.

JACK CHUANG received the Ph.D. degree from The Pennsylvania State University, State College, PA, USA, in 2008, where he was a Graduate Research Assistant with Communications and Space Sciences Laboratory. He then worked with BAE Systems, Merrimack, NH, USA, in electronic warfare and Cisco Systems, Richfield, OH, USA, in spectrum sharing. He is currently with the Communication Technology Laboratory, NIST, Gaithersburg, MD, USA, developing 5G mmWave channel sounders.

RAIED CAROMI received the B.Sc. and M.Sc. degrees in electrical engineering from the University of Mosul, Iraq, in 1999 and 2002, respectively, and the Ph.D. degree in systems engineering from the University of Arkansas at Little Rock in 2014, where he served as a Teaching Assistant with the College of Engineering from 2010 to 2014. In 2013, he worked as an Engineering Intern with WINLAB/Rutgers University, NJ, USA. Since 2015, he has been with the Communications Technology Laboratory, National Institute of Standards and Technology, Gaithersburg, MD, USA. His research interests include cognitive radio, spectrum sharing, RF datasets generation, context-aware wireless communication systems, and applications of machine learning in the next generation wireless communications.

JIAN WANG received the B.S. degree in electrical engineering from Tongji University, Shanghai, China, and the M.S. degree in electrical engineering from Washington State University, Pullman, WA, USA, in 2000. She has been an Electronics Engineer with the Communication Technology Laboratory, National Institute of Standards and Technology, Gaithersburg, MD, USA, since 2015. From 2000 to 2015, she worked in the wireless industry, including Nokia, Irving, TX, USA; Texas Instruments, Dallas, TX, USA; and Digital Receiver Technology Inc., Germantown, MD, USA, on digital signal processing and wireless protocol research and development. Her research interests include next-generation wireless systems, channel modeling, and machine learning.

JELENA SENIC received the B.S. and M.S. degrees in electrical engineering from the University of Belgrade, Serbia, in 2009 and 2010, respectively. Since January 2015, she has been a Researcher with the National Institute of Standards and Technology. Her current research interests include radio propagation channel measurements and modeling at millimeter-wave frequencies. The team in which she works was a recipient of the Best Measurement Paper Award at EuCAP 2017.
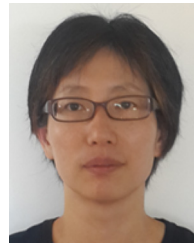
CHIEHPING LAI received the M.S. and the Ph.D. degrees in electrical engineering from The Pennsylvania State University, University Park, in 2004 and 2007, respectively. He is an Electronics Engineer with NIST Communications Technology Laboratory. He is interested in mmwave systems, tracking algorithms, and data processing.

SAMUEL BERWEGER received the Ph.D. degree from the University of Washington, Seattle, WA, USA, in 2011. He joined the National Institute of Standards and Technology (NIST) in 2013. In 2022, he joined the NIST Communications Technology Laboratory to pursue interests in channel sounding and advanced free-space RF propagation measurements. His past research interests were focused on scanning probe-based sub-diffraction limit microscopy at optical and microwave frequencies.

ANURAAG BODI received the B.Tech. degree in electronics and communication engineering from Andhra University, Visakhapatnam, India, in 2012, the first M.S. degree in electrical engineering from the University of Colorado at Boulder in 2016, and the second M.S. degree in computer science from Georgia Tech in 2023. He is also working as a Contractor with the Wireless Networks Division, National Institute of Standards and Technology, Gaithersburg, MD, USA.

WILLIAM SLOANE received the B.E. degree (Hons.) in electrical and electronic engineering from the University of Canterbury (UC), Christchurch, New Zealand, in 2019, where he is currently pursuing the Ph.D. degree in electrical and electronic engineering with Wireless Research Centre. In 2022, he was a Guest Researcher with the National Institute of Standards and Technology, Gaithersburg, MD, USA, as part of the wireless networks division. His current interests include channel modeling for 5G and 6G wireless systems, in particular, the modeling of advanced features for 5G and 6G channels.

CAMILLO GENTILE (Member, IEEE) received the Ph.D. degree in electrical engineering from The Pennsylvania State University, University Park, PA, USA, in 2001. He joined the National Institute of Standards and Technology, Washington, DC, USA, in 2001. He initiated the Radio Access and Propagation Metrology Group, Communications Technology Laboratory in 2021 and led the group until 2023. He is currently leading the NextG Channel Measurement and Modeling Project. He has coauthored over 100 peer-reviewed journal and conference papers, and two books: *Geolocation Techniques* (Springer, 2012) and *Radio Propagation Measurements and Channel Modeling: Best Practices in Millimeter-Wave and Sub-Terahertz Frequencies* (Cambridge University Press, 2022). His recent interests include channel modeling and physical-layer modeling for joint communications and sensing systems.

NADA GOLMIE (Fellow, IEEE) received the Ph.D. degree in computer science from the University of Maryland, College Park, MD, USA. Since 1993, she has been a Research Engineer with the National Institute of Standards and Technology (NIST), Gaithersburg, MD, USA, where she was the Chief of Wireless Networks Division from 2014 to 2022. She is currently a NIST Fellow with the Communications Technology Laboratory. She is the author of *Coexistence in Wireless Networks: Challenges and System-Level Solutions in the Unlicensed Bands* (Cambridge University Press, 2006). Her research interests include media access control and protocols for wireless networks led to more than 200 technical papers presented at professional conferences, journals, and contributed to international standard organizations and industry led consortia. She leads several projects related to the modeling and evaluation of future generation wireless systems and protocols and the NextG Channel Model Alliance Chair.